10-15-2008

Spatiotemporal Patterns in a Langmuir Monolayer Due To Driven Molecular Precession

Satyendra Kumar
Kent State University - Kent Campus, skumar@kent.edu

R. K. Gupta

K. A. Suresh

L. M. Lopatina

R. L. B. Selinger
Kent State University - Kent Campus, rselinge@kent.edu

See next page for additional authors

Authors
Satyendra Kumar, R. K. Gupta, K. A. Suresh, L. M. Lopatina, R. L. B. Selinger, and Jonathan V. Selinger

Spatiotemporal patterns in a Langmuir monolayer due to driven molecular precession

R. K. Gupta, K. A. Suresh,* and S. Kumar
Raman Research Institute, Sadashivanagar, Bangalore 560 080, India

L. M. Lopatina, R. L. B. Selinger, and J. V. Selinger†
Liquid Crystal Institute, Kent State University, Kent, Ohio 44242, USA

(Received 20 October 2007; revised manuscript received 26 May 2008; published 7 October 2008)

Langmuir monolayers of chiral liquid crystals on the surface of water exhibit orientational waves with complex spatiotemporal patterns. These patterns arise from a collective precession of the mesogenic molecules, driven by the evaporation of water through the monolayer. We investigate the behavior of these orientational waves around topological defects in the molecular orientation. Through Brewster angle microscopy, we find that the waves form a reversing spiral pattern, which rotates about the central vortex. With increasing relative humidity, the rotation slows and then stops. We model the system theoretically, and show that predicted patterns are in good agreement with the experiments.

DOI: 10.1103/PhysRevE.78.041703 PACS number(s): 61.30.Jf, 61.30.Dk, 68.18.−g

I. INTRODUCTION

Spatiotemporal patterns like spiral waves and concentric circular stripe waves are ubiquitous in nature, occurring in a wide range of physical, chemical, and biological systems [1–4]. Striped patterns often form in liquid crystals, usually induced by asymmetry in molecular shape, which favors modulation in molecular orientation. Molecular chirality, for instance, can induce stripes or spirals in freely suspended liquid-crystalline films [5,6]. Alternatively, patterning may arise at an interface between two phases due to asymmetry between the phases, as observed at the free surface of liquid crystals [7] and in Langmuir monolayers on the surface of water [8–12].

In a remarkable study, Tabe and Yokoyama [13] reported a surprising new type of nonequilibrium spatiotemporal pattern formation in Langmuir monolayers of chiral mesogenic molecules. They observed that evaporation of water through the monolayer drives the molecules to undergo collective precession of their tilt orientation. These precessing molecules may be regarded as synthetic molecular motors, of interest due to their potential to perform biological and chemical functions. If boundary conditions pin the tilt orientation along a domain wall, the collective precession induces the formation of stripes in this orientation, which accumulate against the wall. Unlike the equilibrium stripes seen earlier, these nonequilibrium stripe patterns evolve in time.

Apart from these nonequilbrium stripe patterns, Langmuir monolayers *also* exhibit vortices, topological defects about which the molecular tilt rotates through 360°. An interesting question is how the nonequilibrium stripe pattern interacts with topological defects. Recently, Svenšek *et al.* predicted that a vortex transforms the stripe pattern into a spiral wave [14]. However, so far such spatiotemporal spiral patterns have not been observed experimentally.

In this paper, we present experimental and theoretical studies of Langmuir monolayers of chiral mesogenic molecules on the surface of water. We find that the monolayers exhibit four phases: a gas phase, a low-density liquidlike phase with varying tilt azimuth of the molecules, a relatively high density liquid phase with tilted molecules, and a condensed phase with untilted molecules. In the low density liquidlike phase, our Brewster angle microscope (BAM) images reveal patterns of linear stripes, concentric circular stripes, and spirals that rotate with time. The rotation rate decreases with increasing relative humidity, that is, with decreasing rate of water evaporation. We also present a theoretical pattern formation model which goes beyond earlier theoretical work by considering finite-strength anchoring along domain walls, unequal Frank constants, and complex geometries. The model predicts spiral patterns that are in good agreement with experimental results.

II. EXPERIMENT

We used 6-(cholest-5-ene-3-lyoxy)-6-oxohexanoic acid [15] (cholesteric acid), synthesized in our laboratory. The purity was checked by NMR and other techniques, and was estimated to be better than 99%. The structure of cholesteric acid (ChA) is shown in Fig. 1. ChA exhibits a cholesteric phase in the range of 146.7–148.5 °C on heating. The molecule shows a right-handed specific optical rotation of +232°. A solution at concentration 1.94 mM in HPLC grade chloroform was used to form the monolayer at the air-water interface. The water used in the experiments was ultrapure ion-free having a resistivity greater than 18 MΩ cm obtained by passing double distilled water through the filtering and deionizing columns of a Milli-Q Millipore unit. The monolayer was formed in a Langmuir trough (NIMA 611M) by spreading the solution of the sample onto the ion-free water using a microsyringe (Hamilton). About 10 min were allowed for the solvent to evaporate from the water surface leaving behind the dispersed molecules. The monolayer was compressed symmetrically between the two coupled barriers of the trough at the rate of 5.14 (Å^2/molecule)/min. The trough was housed in a Plexiglas box to prevent any thermal and air drift. The monolayer was observed using Brewster

*suresh@clcr.res.in
†jvs@lci.kent.edu

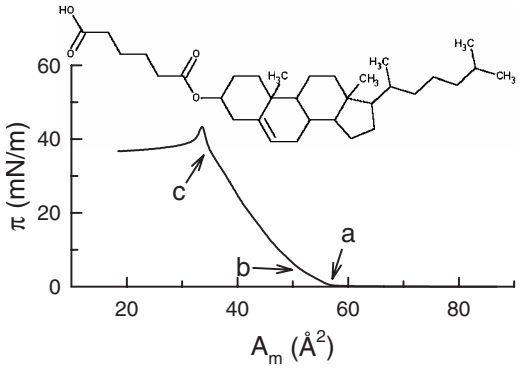

FIG. 1. Surface pressure (π)–area per molecule (A_m) isotherm of cholesteric acid (ChA) monolayer at the air-water interface. Kinks in the isotherm are denoted by arrows at **a** (A_m=57 Å^2), **b** (A_m=52 Å^2), and **c** (A_m=35 Å^2). Inset: Chemical structure of the ChA molecule.

angle microscope (BAM) and epifluorescence microscope. The Brewster angle microscope (MiniBAM, Nanofilm Technologie) was equipped with a 30-mW 660-nm laser and a charge-coupled device (CCD) camera. In epifluorescence microscopy, the monolayer was doped with an amphiphilic fluorescent probe, 4-(hexadecylamino)-7-nitrobenz-2 oxa-1,3 diazole (Molecular Probes) of concentration of about 1% in the monolayer. The dye doped monolayer was observed under a Leitz Metallux 3 epifluorescence microscope. The images were monitored and captured using an intensified CCD camera (Cairn Research), and they were digitized using a frame grabber. The temporal evolution of the patterns was studied by capturing the sequence of images at an interval of one frame per second using a program written in LABVIEW. The captured images were analyzed using MATLAB. The relative humidity was increased by placing water in Petri dishes inside the Plexiglas box, and it was reduced by replacing water with dry $CaCl_2$. The experiments were carried out at room temperature ($\approx$24 °C) and a relative humidity of 60% unless otherwise stated.

The surface pressure (π)–area per molecule (A_m) isotherm of the ChA monolayer at the air-water interface is shown in Fig. 1. It reveals three kinks, indicating three phase transitions. The monolayer collapses at 33.8 Å with a collapse pressure (π_c) of 43.5 mN/m. In the isotherm, extrapolating the regions **a**-**b**, **b**-**c**, and **c**-collapse, to zero surface pressure yields the limiting areas of 56.5, 51.0, and 40.0 Å^2, respectively. The monolayer was very stable and showed no hysteresis on expansion.

The BAM images of the ChA monolayer at the air-water interface are shown in Fig. 2. At large A_m [Fig. 2(a)], the monolayer shows a coexistence of dark region and gray background with stripelike patterns. The dark region corresponds to the gas (G) phase. The patterns consist of linear stripes, concentric circular stripes, and spirals [Fig. 2(b)]. The patterns vanish on compression, leading to a very uniform gray texture. On further compression, the monolayer collapses with the appearance of three-dimensional (3D) domains.

There is strong evidence that the monolayer phase with stripe patterns is a tilted liquidlike phase. First, in this phase

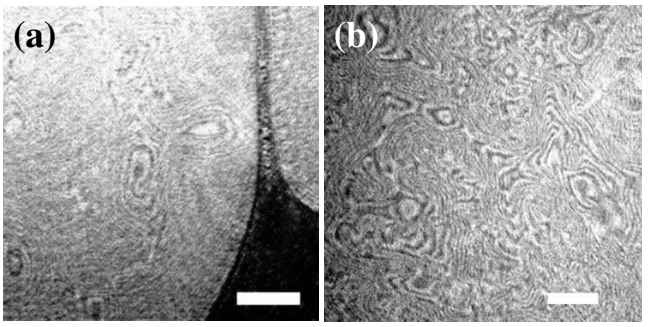

FIG. 2. BAM images of the ChA monolayer at the air-water interface: (a) Coexistence of dark region and gray domains with stripe patterns (A_m=87.0 Å^2). (b) Stripe patterns on gray background (A_m=54.7 Å^2). Scale bar=500 μm.

the monolayer appears very mobile, implying a liquidlike structure. Moreover, the A_m value for the normally oriented ChA molecules in the monolayer is around 40 Å^2. The large limiting A_m (56.5 Å^2) corresponding to the region **a**-**b** (Fig. 1) can be accounted for by the tilt of the molecules in the monolayer. In the ChA molecule, the size of the carboxylic polar group is around 2 Å, whereas the sterol nonpolar group is around 5 Å. Size mismatch of the polar and nonpolar groups is known to induce a tilt of the molecules in the monolayer [8,9,16]. Hence we identify this phase as the L_1' phase.

Earlier studies have shown that intensity modulation in BAM images can be caused by variations in the molecular tilt azimuth, as well as variations in the density [17,18]. To determine which mechanism causes the observed patterns in our BAM images of the L_1' phase, we dissolve a dye in the monolayer and take epifluorescence microscope images, as shown in Fig. 3(a). The miscibility of dye in a Langmuir monolayer phase is dependent on the surface density of the phase [19]. Therefore any density variation would have led to a variation in the fluorescence intensity. The absence of such variation in the fluorescence intensity of Fig. 3(a) suggests that the formation of stripes and spirals in the BAM images is due to a tilt-azimuthal variation rather than a density variation. Tabe *et al.* have shown that simultaneous imaging of a monolayer using a linear- and circular-depolarized reflected light microscope (DRLM) yields information on the tilt and azimuthal variation of the molecules in the monolayer [20]. The tilt and the azimuthal variation were extracted

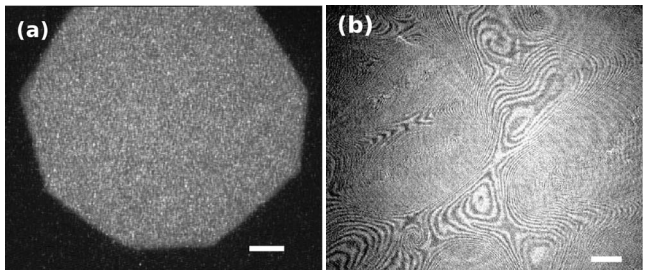

FIG. 3. (a) ChA monolayer, epifluorescence image at A_m =54 Å^2. The gray uniform texture represents the uniform L_1' phase. Scale bar=312 μm. (b) BAM image at the same A_m, after 24 h at π=2.4 mN/m. Scale bar=500 μm.

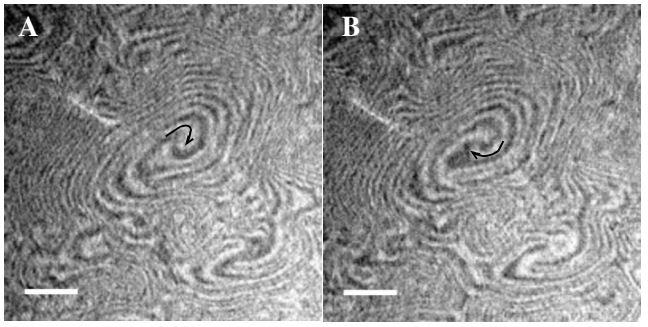

FIG. 4. BAM images at A_m=54 Å^2, four minutes after compression to surface pressure=2.4 mN/m. Time between images=2 sec; arrows show rotation sense. Scale bar=335 μm.

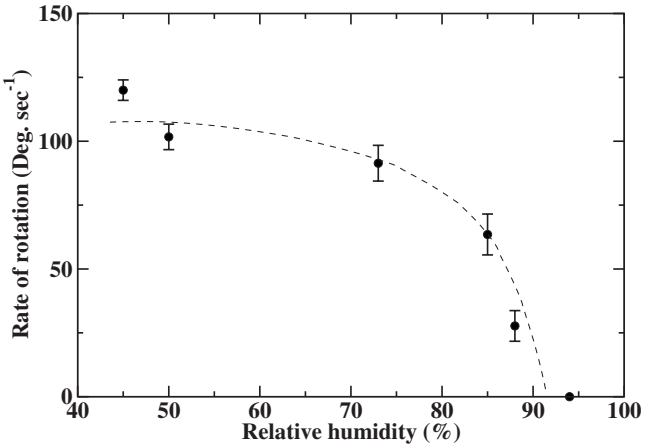

FIG. 5. Spiral rotation rate as a function of relative humidity. The points represent the experimental data, and the dashed line is a guide to the eye.

from the intensity data of circular and linear DRLM, respectively [21]. The geometry of our BAM imaging is similar to that reported for the linear DRLM except that the angle of incidence in their case is 20° [20], whereas in BAM it is the Brewster angle (~53°) for the air-water interface. Hence the intensity variation in our BAM images can be attributed to the variation of the azimuthal angle of the tilted molecules.

The phase corresponding to the region **b**-**c** (Fig. 1) shows a large limiting A_m value of 51.0 Å^2, suggesting a tilt of the molecules in the monolayer in this phase. However, unlike the L_1' phase, a uniform texture is seen in the BAM images. The images also indicate a liquidlike phase. Hence this phase may be regarded as a high-density liquid phase with tilted molecules. We have identified this phase as the L_2' phase. The phase corresponding to the region **c**-collapse (Fig. 1) yields the limiting A_m value of 40 Å^2. This value approximately corresponds to the cross-sectional area of the molecule in the normal orientation. BAM images in this phase also exhibit a uniform texture. Therefore this phase can be regarded as a condensed phase with untilted molecules (L_2 phase).

The patterns observed in the L_1' phase vary with time. Immediately after compression to the L_1' phase, a few stripes and small spirals form. The number of stripes and the size of the spirals grow with time. Figure 3(b) shows well-developed spirals and stripes seen after 24 h. The stripe width varies from 20 to 100 μm. Furthermore, the spirals rotate with time. Figure 4 presents BAM images for ChA in the L_1' phase at two different times, showing right-handed (clockwise) rotation of the spirals; the corresponding movie is presented in EPAPS [22]. This rotation can be related to the molecular chirality. It is reminiscent of the effect of molecular chirality on the shapes of liquid-condensed domains in Langmuir monolayers of dipalmitoyl phosphatidylcholine (DPPC), as studied by Krüger and Lösche [23]. They observed right- and left-handed spiral structures for L-DPPC and D-DPPC, respectively.

In further experiments, we have studied pattern evolution in the L_1' phase as a function of relative humidity in the air above the monolayer. As the humidity increases, the dynamics associated with the patterns slows down, and the spiral rotation rate decreases, as shown in Fig. 5 and in movies on EPAPS [22]. The rotation rate decreases sharply above 70% and approaches zero at 94% relative humidity. To understand these results, note that the increase in humidity decreases the concentration gradient of water across the interface, which lowers the evaporation rate and thus reduces the driving force for rotation. Note also that the *shape* of the spirals becomes distorted as the humidity increases. This trend is reasonable, because thermal noise must dominate as the driving force is reduced, leading to irregularly shaped spirals. The simulations of Svenšek *et al.* [14] have shown this trend for increasing magnitude of the noise.

III. THEORY

As argued by Tabe and Yokoyama [13], the spatiotemporal patterns arise due to collective precession of chiral molecules at the air-water interface, driven by transfer of water across the monolayer during evaporation through a process related to Lehmann rotation. The optimal frequency of molecular precession depends linearly on the concentration gradient of water across the interface, and on the molecular chirality. If the monolayer were uniform, with no boundaries, domain walls, or topological defects, then all molecules would precess with the same frequency and no patterns would form. However, if there are nonuniformities in the monolayer, then there are nontrivial boundary conditions on the director, which can lead to complex patterns.

Precession of the molecules, in the absence of flow, can be described by the equation of motion [13,14]

$$\frac{\partial \varphi}{\partial t} = -\frac{1}{\gamma}\frac{\delta F}{\delta \varphi(\mathbf{r},t)} + \omega_L, \tag{1}$$

where $\varphi(\mathbf{r},t)$ is the azimuthal angle of the in-plane director, F is the elastic free energy, γ is the rotational viscosity, and ω_L is the external driving due to evaporation. (The sign of ω_L depends on the chirality of the molecules.) Earlier studies used the approximate free energy with a single Frank constant

$$F = \int d^2\mathbf{r}\frac{1}{2}K|\nabla\varphi|^2, \tag{2}$$

in which case the equation of motion reduces to the driven diffusion equation

$$\frac{\partial \varphi}{\partial t} = \frac{K}{\gamma}\nabla^2 \varphi + \omega_L. \tag{3}$$

As shown in earlier work, this approach explains the formation of stripes near straight walls with infinitely strong anchoring [13], and it predicts spirals around topological defects in a square lattice model [14].

To compare the theoretical prediction with the experimental results, it is helpful to have an analytic solution for the structure and dynamics of a spiral pattern. As a preliminary calculation, we can model a single vortex by solving the equation of motion (3) in an annular ring $r_{\min} < r < r_{\max}$, using polar coordinates (r, θ). For the moment, let us consider rigid boundary conditions that require a single vortex with topological charge of +1 at the origin

$$\varphi(r_{\min}, \theta, t) = \varphi(r_{\max}, \theta, t) = \theta + \frac{\pi}{2}. \tag{4}$$

The boundary condition at $r_{\max}$ represents rigid anchoring of the director along an outer domain wall, while the boundary condition at $r_{\min}$ describes rigid anchoring along a dust particle or other inclusion. The initial condition is the lowest-energy equilibrium state around a vortex,

$$\varphi(r, \theta, 0) = \theta + \frac{\pi}{2}. \tag{5}$$

The equation of motion (3) can then be solved analytically as a series of Bessel functions,

$$\varphi(r,\theta,t) = -\frac{\gamma\omega_L}{4K}r^2 + C_1 \ln r + C_2 + \theta + \frac{\pi}{2} + \sum_{i=1}^{\infty} D_i e^{-(K/\gamma)k_i^2 t}\left(\frac{J_o(k_i r)}{J_o(k_i r_{\min})} - \frac{Y_o(k_i r)}{Y_o(k_i r_{\min})}\right), \tag{6}$$

where the C, D, and k coefficients can be expressed in terms of $r_{\min}$ and $r_{\max}$.

For short times $t \ll \gamma r_{\max}^2/K$, the dynamic solution of Eq. (6) shows a spiral pattern that gradually rotates and winds up, consistent with the experimental BAM videos. For long times $t \gg \gamma r_{\max}^2/K$, the dynamic solution asymptotically approaches a steady-state limit, at which the rotation slows to a halt. At this point, the elastic torque due to the rigid surface anchoring cancels the Lehmann torque due to evaporation, and the system reaches a stable mechanical equilibrium.

Figure 6(b) shows the director field corresponding to the final state at $t \to \infty$ (visualized using an equation of Tabe and Yokoyama [13,21] for the optical intensity as a function of azimuthal angle). Note that this texture has a spiral pattern with an interesting reversing structure, which goes in one direction near the inner boundary (the vortex core) and the opposite direction near the outer boundary (the surrounding domain wall). This reversing structure can be understood because the molecules cannot rotate at the inner and outer boundaries, and hence the maximum rotation must occur between the two boundaries. The maximum corresponds to the reversal point. This theoretical prediction is generally consistent with the experimentally obtained pattern shown in Fig. 6(a), although the reversal is more pronounced in the prediction than in the experiment.

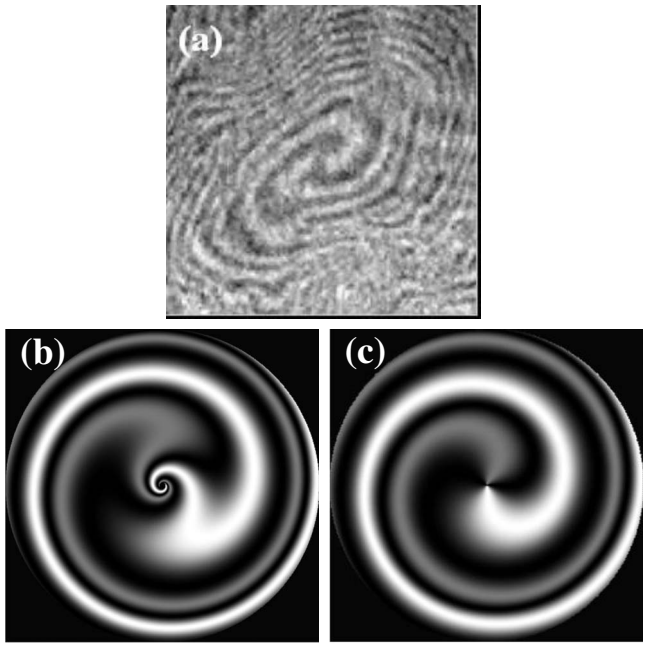

FIG. 6. Spiral patterns for a single vortex surrounded by a domain wall: (a) Experimentally observed BAM image (size of full image=1100 μm). (b) Theoretical prediction for the preliminary single-Frank-constant approximation, with rigid anchoring on the inner and outer boundaries. (c) Prediction for the case of unequal Frank constants, $K_3/K_1=1.5$. In case (c), the anisotropy of Frank constants gives an effective pinning of the director field at the vortex core, even without any imposed anchoring at the inner boundary.

Although this preliminary solution agrees with several features of the BAM images, there are still three important discrepancies between theory and experiment. First, the theoretical prediction of the reversing spiral pattern involves anchoring on a dust particle or other inclusion at the vortex core. An experimental monolayer might have some particles, but it seems unlikely to have a particle at the center of every spiral. It would be more satisfying to find a theoretical explanation that does not require such particles. Second, the theoretical prediction always relaxes toward a steady state, at which all rotation slows to a halt. By contrast, the experimental patterns only reach a steady state if the relative humidity is sufficiently high; otherwise the spiral rotation continues indefinitely. We would like to understand how this indefinite rotation can occur. Third, the theoretical prediction only applies to a single vortex in a circular geometry, while the experiments show complex textures of spirals and stripes over long length scales. We need to supplement the theoretical approach to describe these extended geometries.

To resolve these discrepancies, we must consider three new theoretical issues:

A. Unequal Frank constants

So far, we have assumed that the Frank elastic constants of the monolayer are equal. In general, however, the elastic

constants for splay (K_1) and bend (K_3) are different. This difference is especially important near the vortex core, where director gradients are large. To minimize the elastic free energy, the distortion near the core must be mainly splay or mainly bend, whichever has a lower Frank constant. As a result, the difference $\Delta K = K_3 - K_1$ provides an energy barrier resisting precession at the vortex core. Hence the director field rotates in the domain interior but remains fixed near the core until enough elastic strain builds up to overcome the energy barrier. At that point, the director rapidly rotates 180°, reaching the favored splay or bend once again. This behavior is closely analogous to that of vortex unwinding in freely suspended smectic films [24].

For unequal Frank constants, the free energy must be written in terms of the director $\hat{\mathbf{c}} = (\cos\varphi, \sin\varphi)$ as

$$F = \int d^2\mathbf{r}\left[\frac{1}{2}K_1|\nabla\cdot\hat{\mathbf{c}}|^2 + \frac{1}{2}K_3|\nabla\times\hat{\mathbf{c}}|^2\right]. \quad (7)$$

We put this free energy into Eq. (1) to obtain a general nonlinear equation of motion. For a specific example of the resulting behavior, we solve this equation in the annular ring $r_{\min} < r < r_{\max}$. On the outer edge, we impose tangential boundary conditions, $\varphi(r_{\max}, \theta, t) = \theta + \frac{\pi}{2}$, requiring the presence of a vortex. On the inner edge, however, we consider *free* boundary conditions, in order to determine the behavior if there is no dust particle or other inclusion. The monolayer then evolves asymptotically toward a steady state at which $\partial\varphi/\partial t = 0$. Note that finding this steady state is exactly equivalent to minimizing the effective free energy

$$F_{\text{eff}} = \int d^2\mathbf{r}\left[\frac{1}{2}K_1|\nabla\cdot\hat{\mathbf{c}}|^2 + \frac{1}{2}K_3|\nabla\times\hat{\mathbf{c}}|^2 - \gamma\omega_L\varphi\right]; \quad (8)$$

at the minimum there is a balance between elastic and evaporative torques.

To calculate the steady state, we assume circular symmetry, so that

$$\varphi(r,\theta) = \tilde{\varphi}(r) + \theta + \frac{\pi}{2}. \quad (9)$$

The radial dependence $\tilde{\varphi}(r)$ is then given by the Euler-Lagrange equation

$$\left(1 - \frac{\Delta K\cos[2\tilde{\varphi}(r)]}{2K}\right)\left(\tilde{\varphi}''(r) + \frac{\tilde{\varphi}'(r)}{r}\right) + \frac{\Delta K\sin[2\tilde{\varphi}(r)]}{2K}\left(\tilde{\varphi}'(r)^2 + \frac{1}{r^2}\right) = -\frac{\gamma\omega_L}{K}, \quad (10)$$

where $K = (K_1 + K_3)/2$, with the boundary condition $\tilde{\varphi}(r_{\max}) = 0$. Note that this equation has one undefined parameter, which corresponds to the free boundary condition. To determine this parameter, we solve the differential equation numerically in MATHEMATICA for specified values of the slope $\tilde{\varphi}'(r_{\max})$. We then choose the slope that minimizes the effective free energy F_{eff}.

Figure 7 shows plots of the steady-state solution for $\tilde{\varphi}(r)$, with $K_3/K_1 = 1.5$, for several values of ω_L. Note that $\tilde{\varphi}'(r_{\max}) = 0$, as required by the boundary conditions. By contrast, $\tilde{\varphi}'(r_{\min})$ is approximately a half integer multiple of π,

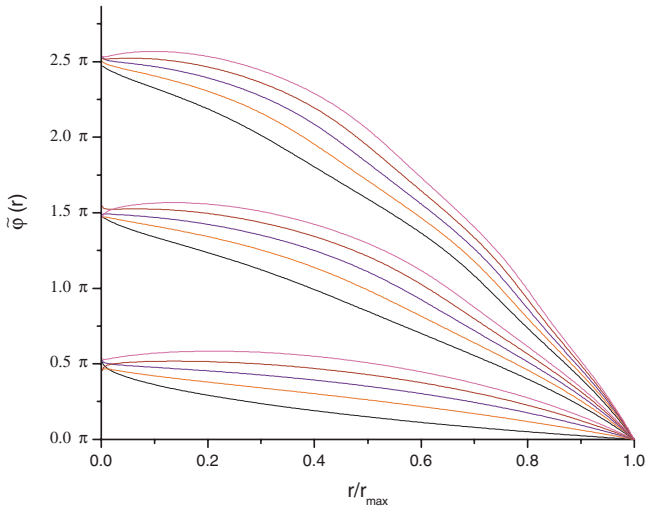

FIG. 7. (Color online) Plots of the director orientation $\tilde{\varphi}(r)$, for infinite anchoring on the outer boundary and no anchoring on the inner boundary. The elastic anisotropy is $K_3/K_1 = 1.5$ and radius is $r_{\max} = 5$, with $\gamma\omega_L/K = 0 - 1.4$, in steps of 0.1, from bottom to top.

so that the elastic distortion near the vortex is almost entirely splay rather than bend. As ω_L increases, there is a greater director rotation within the bulk of the domain. When this bulk realignment becomes large enough, $\tilde{\varphi}'(r_{\min})$ jumps from one half integer multiple of π to the next, in order to reduce the bulk elastic distortion. Thus the anisotropy of elastic constants gives an effective finite-strength anchoring of the director orientation at $r_{\min}$, even without any dust particle or other boundary energy there. Note also that the slope $\tilde{\varphi}'(r_{\min})$ may be either positive or negative. Although free boundary conditions require $\tilde{\varphi}'(r_{\min}) = 0$ in *linear* systems, that boundary condition does not occur in this *nonlinear* system.

Each plot of the radial solution $\tilde{\varphi}(r)$ corresponds to a 2D plot of the optical intensity as a function of position. For example, Fig. 6(c) shows the prediction for $\gamma\omega_L/K = 1.4$. Note that the bulk region with $\tilde{\varphi}'(r_{\min}) < 0$ corresponds to a spiral with forward twist, but the smaller region with $\tilde{\varphi}'(r_{\min}) > 0$ corresponds to a spiral with reverse twist near the central vortex. Thus the anisotropy of Frank constants induces this reverse twist for some ranges of ω_L, while other values of ω_L give only forward twist. The reverse twist induced by this mechanism in Fig. 6(c) is not as pronounced as the reverse twist induced by strong anchoring at the vortex core in Fig. 6(b), but it is still noticeable, and it compares well with the experimental image in Fig. 6(a).

B. Finite-strength anchoring

Along the outer edge of a domain, an anchoring potential tends to align the director with respect to the domain wall. At this anchoring surface, molecular precession is hindered and the system builds up elastic strain. If the anchoring is infinitely strong, as assumed in earlier studies, then the elastic torque eventually cancels the torque due to evaporation, and the system reaches a *stable* mechanical equilibrium, with no further precession. However, if the anchoring strength is only

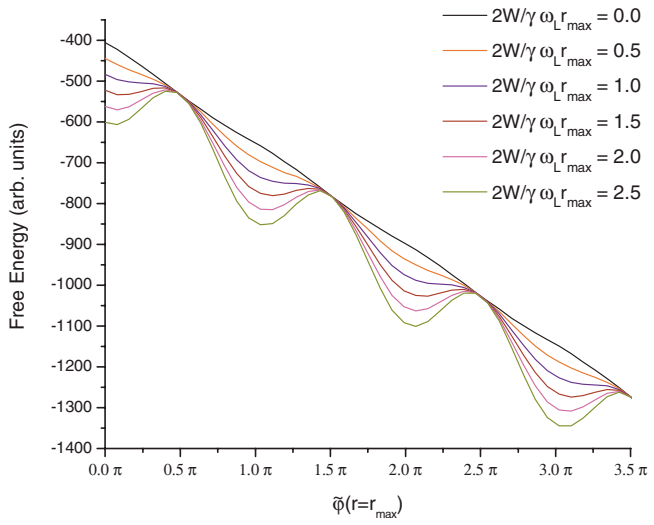

FIG. 8. (Color online) Plots of the total free energy F_{total} as a function of $\tilde{\varphi}(r_{\max})$ for several values of the anchoring strength W, with $K_3/K_1=1.5$, $r_{\max}=5$, and $\gamma\omega_L/K=0.5$.

finite, the behavior may be more complex. The question is then: Can the system reach any state that is even *metastable*, or does the director field just precess indefinitely without stopping?

To answer this question, we must modify the model by eliminating the boundary condition at the outer edge of the domain. Instead, we use an anchoring energy of the form $F_{\text{anchor}}=-W(\hat{\mathbf{c}}\cdot\hat{\mathbf{t}})^2$, where $\hat{\mathbf{t}}$ is a unit vector tangent to the domain wall. Assuming the circular symmetry of Eq. (9), the anchoring energy becomes simply $F_{\text{anchor}}=-W\cos^2\tilde{\varphi}(r_{\max})$. We must now determine whether this anchoring is strong enough to hold the system at a particular value of $\tilde{\varphi}(r_{\max})$. To do so, we solve the Euler-Lagrange equation of Eq. (10) for particular values of $\tilde{\varphi}(r_{\max})$ and $\tilde{\varphi}'(r_{\max})$, and use this solution to obtain the total free energy $F_{\text{total}}=F_{\text{eff}}+F_{\text{anchor}}$ as a function of $\tilde{\varphi}(r_{\max})$ and $\tilde{\varphi}'(r_{\max})$. We then minimize this total free energy over $\tilde{\varphi}'(r_{\max})$ to obtain F_{total} in terms of $\tilde{\varphi}(r_{\max})$ alone.

Figure 8 shows plots of F_{total} as a function of $\tilde{\varphi}(r_{\max})$ for several values of the anchoring strength W. These plots show that the system with finite anchoring can have no equilibrium that is truly stable; rotating the director through an angle of 2π is always favored. Rather, there are two possible types of behavior. If the anchoring is sufficiently strong, then the system reaches a metastable equilibium, in which all torques cancel. In that metastable state, the system must get over an energy barrier before it can precess further. By contrast, if the anchoring is not sufficiently strong, then it cannot cancel the evaporative torque, and hence there is not even a metastable state. Instead, the director field precesses continuously, in a dynamic striped or spiral pattern.

In the limit of equal Frank constants and $r_{\max}\gg r_{\min}$, the threshold between these two types of behavior occurs at an anchoring strength of $W=\gamma\omega_L r_{\max}/2$, or equivalently, at a Lehmann rotation of $\omega_L=2W/(\gamma r_{\max})$. In the general case of unequal Frank constants, the threshold is shifted slightly from that value. This result is at least qualitatively consistent with our experimental observation of the spiral rotation rate

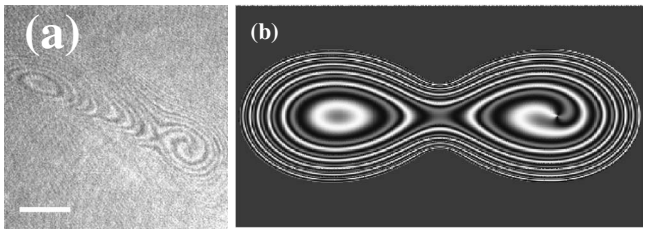

FIG. 9. (a) Experimental BAM image (scale bar=500 μm) and (b) simulated defect pattern in an extended domain.

as a function of relative humidity, as shown in Fig. 5. For low relative humidity, the Lehmann rotation ω_L is high, presumably above this threshold. For that reason, the anchoring along the domain walls is not strong enough to hold the system in a metastable state, and hence the spirals rotate indefinitely. For high relative humidity, the Lehmann rotation ω_L is lower. Once it goes beyond the threshold, the domain wall anchoring can lock the system in a metastable state, and hence the spiral rotation rate goes to zero.

C. Complex geometries

So far, we have only modeled monolayer domains with circular shapes. However, actual monolayers generally have much more complex geometries. In typical experiments, monolayers exhibit many domains of a tilted phase surrounded by defect walls and by regions of an untilted phase. The boundary conditions on any closed domain will favor the presence of a vortex in the molecular tilt, with a topological charge of +1. The corresponding antivortices will be pushed into the domain walls or hidden in the regions of untilted phase, so that they do not appear in the tilted do-

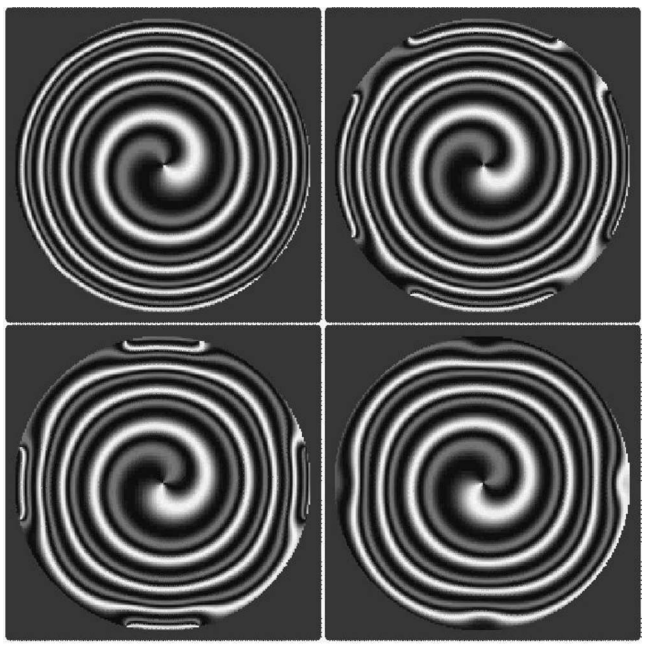

FIG. 10. Snapshots from a lattice simulation of a domain with finite anchoring energy, showing the creation, motion, and annihilation of four dislocation pairs.

mains. Thus only positively charged vortices will be present to interact with the precessing tilted molecules to form spirals. This scenario explains the experimental observation of spirals with only one handedness.

To model the spatiotemporal patterns in complex geometries, we perform numerical simulations of a lattice model of the monolayers. In these simulations, we discretize the monolayer on a hexagonal lattice, with an arbitrarily shaped closed boundary that requires the presence of a single vortex in the molecular tilt. We then solve for the time-dependent director field $\varphi(\mathbf{r},t)$ by iterating the equation of motion (1) numerically, approximating all gradients by finite differences between lattice sites. In these simulations, we consider the case of unequal Frank constants $K_3/K_1=1.5$.

For a specific example of an extended geometry, we consider a double-lobed domain with one vortex and infinitely strong surface anchoring. The resulting pattern, in the middle of the relaxation process, is shown in Fig. 9(b). A spiral forms around the vortex, while the other side of the domain shows concentric circles around a defect-free interior. This image is consistent with the experimental pattern in Fig. 9(a).

As a final point, the simulation model can also provide information about the role of defects in the dynamic evolution of the spatiotemporal patterns. In the previous section, we showed that a domain with finite anchoring energy can have a series of metastable states, separated by energy barriers. In that calculation, we considered only circularly symmetric states, and thus assumed that the only way to transform from one metastable state to the next is by rotating the director *everywhere* along the domain wall. However, the energy barrier against this rotation can be very high. A much lower-energy pathway to go from one metastable state to another is by generating pairs of dislocations in the striped pattern, letting the dislocations move around the domain perimeter, and allowing dislocation pairs to annihilate. This behavior occurs in simulations of domains with finite anchoring energy. For example, Fig. 10 presents a series of snapshots from one simulation, showing the creation, motion, and annihilation of four dislocation pairs. This process eliminates one stripe from the pattern, thus taking the system out of a metastable state and allowing further precession to occur. Additional experiments are needed to see if this process occurs in ChA monolayers.

In conclusion, Tabe and Yokoyama [13] have shown that evaporation across a Langmuir monolayer can drive collective molecular precession, leading to spatiotemporal stripe patterns. Svenšek *et al.* [14] have simulated the patterns and predicted spiral waves due to vortices in the monolayer. We have now observed spiral waves in monolayers of ChA, and have demonstrated that the spiral rotation rate depends on the evaporation rate. Furthermore, we have modeled the patterns by considering three theoretical issues: unequal Frank constants, finite anchoring, and extended domain shapes. With these new considerations, we find good agreement between experimental observations and theoretical predictions.

[1] A. N. Zaikin and A. M. Zhabotinsky, Nature (London) **225**, 535 (1970).
[2] K. I. Agladge and V. I. Krinsky, Nature (London) **296**, 424 (1982).
[3] V. Pérez-Muñuzuri, R. Aleiv, B. Vasiev, V. Perez-Villar, and V. I. Krinsky, Nature (London) **353**, 740 (1999).
[4] V. K. Vanag and I. R. Epstein, Science **294**, 835 (2001).
[5] S. A. Langer and J. P. Sethna, Phys. Rev. A **34**, 5035 (1986).
[6] S. B. Dierker, R. Pindak, and R. B. Meyer, Phys. Rev. Lett. **56**, 1819 (1986).
[7] R. B. Meyer and P. S. Pershan, Solid State Commun. **13**, 989 (1973).
[8] X. Qiu, J. Ruiz-Garcia, K. J. Stine, C. M. Knobler, and J. V. Selinger, Phys. Rev. Lett. **67**, 703 (1991).
[9] S. Rivière, S. Hénon, and J. Meunier, Phys. Rev. E **49**, 1375 (1994).
[10] Y. Tabe and H. Yokoyama, J. Phys. Soc. Jpn. **63**, 2472 (1994).
[11] J.-L. Gallani, S. Mery, Y. Galerne, and D. Guillon, J. Phys. Chem. B **108**, 11627 (2004).
[12] J. V. Selinger and R. L. B. Selinger, Phys. Rev. E **51**, R860 (1995).
[13] Y. Tabe and H. Yokoyama, Nature Mater. **2**, 806 (2003).
[14] D. Svenšek, H. Pleiner, and H. R. Brand, Phys. Rev. Lett. **96**, 140601 (2006).
[15] J-W Lee, J-I Jin, M. F. Achard, and F. Hardouin, Liq. Cryst. **28**, 663 (2001).
[16] S. A. Safran, M. O. Robbins, and S. Garoff, Phys. Rev. A **33**, 2186 (1986).
[17] J. Meunier, Colloids Surf., A **171**, 33 (2000).
[18] J. Ignes-Mullol and D. K. Schwartz, Nature (London) **410**, 348 (2001).
[19] C. M. Knobler, Science **249**, 870 (1990).
[20] Y. Tabe, N. Shen, E. Mazur, and H. Yokoyama, Phys. Rev. Lett. **82**, 759 (1999).
[21] Y. Tabe and H. Yokoyama, Langmuir **11**, 699 (1995).
[22] See EPAPS Document No. E-PLEEE8-78-044810 for experimental movies of the monolayer dynamics under conditions of different relative humidity. For more information on EPAPS, see http://www.aip.org/pubservs/epaps.html.
[23] P. Krüger and M. Lösche, Phys. Rev. E **62**, 7031 (2000).
[24] A. Eremin, C. Bohley, and R. Stannarius, Phys. Rev. E **74**, 040701(R) (2006); Eur. Phys. J. E **21**, 57 (2006).